

# JGR Atmospheres

## RESEARCH ARTICLE

10.1029/2018JD030044

### Key Points:

- Based on UVES spectra and WACCM/SABER/OSIRIS data, the first comprehensive study of potassium nightglow was performed
- Potassium nightglow shows very different variability compared to sodium nightglow
- The quantum yield of about 30% for potassium nightglow is much higher than for sodium nightglow

### Supporting Information:

- Supporting Information S1
- Data Set S1

### Correspondence to:

S. Noll,  
stefan.noll@dlr.de

### Citation:







Noll, S., Plane, J. M. C., Feng, W., Proxauf, B., Kimeswenger, S., & Kausch, W. (2019). Observations and modeling of potassium emission in the terrestrial nightglow. *Journal of Geophysical Research: Atmospheres*, 124. <https://doi.org/10.1029/2018JD030044>

Received 22 NOV 2018

Accepted 2 MAY 2019

Accepted article online 16 MAY 2019

## Observations and Modeling of Potassium Emission in the Terrestrial Nightglow

S. Noll<sup>1,2</sup> , J. M. C. Plane<sup>3</sup> , W. Feng<sup>3,4</sup> , B. Proxauf<sup>5</sup> , S. Kimeswenger<sup>6,7</sup> ,  
and W. Kausch<sup>6</sup> 

<sup>1</sup>Institut für Physik, Universität Augsburg, Augsburg, Germany, <sup>2</sup>Deutsches Fernerkundungsdatenzentrum, Deutsches Zentrum für Luft- und Raumfahrt, Weßling-Oberpfaffenhofen, Germany, <sup>3</sup>School of Chemistry, University of Leeds, Leeds, United Kingdom, <sup>4</sup>National Centre for Atmospheric Science, University of Leeds, Leeds, United Kingdom, <sup>5</sup>Max-Planck-Institut für Sonnensystemforschung, Göttingen, Germany, <sup>6</sup>Institut für Astro- und Teilchenphysik, Universität Innsbruck, Innsbruck, Austria, <sup>7</sup>Instituto de Astronomía, Universidad Católica del Norte, Antofagasta, Chile

**Abstract** The ablation of cosmic dust entering the atmosphere causes the formation of an atomic potassium (K) layer in the mesopause region. It can be studied via resonance fluorescence from the  $K(D_1)$  line at 769.9 nm, stimulated by sunlight or a laser. In addition, the faint emission from a chemiluminescent cycle involving ozone and oxygen atoms has been observed with a nocturnal mean intensity of about 1 Rayleigh. In this study, the K nightglow is investigated in much greater detail, using 2,299 high-resolution spectra taken with the astronomical echelle spectrograph Ultraviolet and Visual Echelle Spectrograph at Cerro Paranal in Chile (24.6°S) between 2000 and 2014. The seasonal variation is dominated by a maximum in June. During the night, the highest intensities are found close to sunrise. Moreover, there is a clear negative correlation with solar activity. These variations are very different from those of the well-studied sodium (Na) nightglow. The K nightglow at Cerro Paranal was also simulated with the Whole Atmosphere Community Climate Model including K chemistry. The observed and modeled climatologies do not match well, largely because of unreliable Whole Atmosphere Community Climate Model ozone densities. Satellite-based profile retrievals for ozone and temperature from Sounding of the Atmosphere using Broadband Emission Radiometry and K from Optical Spectrograph and Infrared Imaging System were then used to simulate the K nightglow and to derive the quantum yield of the  $K(D)$  emission with respect to the reaction of K with ozone. Considering that the obscured  $K(D_2)$  line is expected on theoretical grounds to be 1.67 times brighter than  $K(D_1)$ , we find about 30% for this quantum yield, which is much higher than for Na(D) emission.

### 1. Introduction

The continuous input of meteoric material into the Earth's atmosphere and the subsequent ablation processes and chemical reactions cause the formation of various metal layers with typical heights of their density maxima between 85 and 95 km (Plane, 2012; Plane et al., 2015). The column density and structure of these layers show variations on different timescales. In this respect, the variability of the potassium (K) layer is different from that of sodium (Na), the next lighter alkali metal. While Na exhibits a dominant annual oscillation (AO) with a maximum in late autumn/early winter in both hemispheres at nonequatorial latitudes (Fan et al., 2007; Gardner et al., 2005; Langowski et al., 2017; States & Gardner, 1999; Yi et al., 2009), the K layer at all latitudes is characterized by a pronounced semiannual oscillation (SAO) with maxima around the solstices (Dawkins et al., 2015; Eska et al., 1998; Friedman et al., 2002; Lautenbach et al., 2017; Wang et al., 2017; Yue et al., 2017). Plane et al. (2014) explain these differences by a nearly temperature-independent cycling between K and the main neutral reservoir species  $KHCO_3$ . Photolysis of the latter is much more important than the strongly temperature-dependent reaction with atomic hydrogen. In contrast, the activation energy for the reaction of  $NaHCO_3$  with atomic hydrogen yielding Na and  $H_2CO_3$  is small enough to be significant at the low temperatures of the upper mesosphere. Moreover, the production of K by the dissociative recombination of  $K^+$  clusters is only efficient at very low temperatures (typical of the high-latitude summer). The formation of such clusters is less efficient than in the case of  $Na^+$  due to the larger  $K^+$  ion.

Our knowledge of the K chemistry in the mesopause region and the variability of the concentrations of the K-related species is essentially based on the observation of the fluorescent emission of the  $K(D_1)$  line at

769.9 nm (in air)



which connects the electronically excited state  $^2P_{1/2}$  with the ground state  $^2S_{1/2}$ . The probably stronger  $K(D_2)$  line at 766.5 nm



originating from  $^2P_{3/2}$  cannot be used as it is strongly affected by absorption and emission of  $O_2(b-X)(0-0)$ , the Fraunhofer A-band (Dawkins et al., 2014; Slanger & Osterbrock, 2000).  $K(D_1)$  radiation stimulated by solar photons was first discovered under twilight conditions by Sullivan and Hunten (1962). Since the first use of laser light for its activation by Felix et al. (1973), the lidar technique is the preferred method for ground-based studies of the K layer. Nevertheless, observations extending for more than a year are limited to a few stations in the Northern Hemisphere: Longyearbyen at 78°N (Höffner & Lübken, 2007), Kühlungsborn at 54°N (Lautenbach et al., 2017; von Zahn & Höffner, 1996; Eska et al., 1998), Beijing at 40°N (Wang et al., 2017), and Arecibo at 18°N (Friedman et al., 2002; Yue et al., 2017). In addition, nearly global daytime retrievals of the K layer density profile were obtained from  $K(D_1)$  resonance fluorescence measurements made by the limb-scanning Optical Spectrograph and Infrared Imaging System (OSIRIS) onboard the Odin satellite for the period from 2004 to 2013 (Dawkins et al., 2014, 2015).

Another way to study the chemistry of alkali metals in the mesopause region is the observation of D-line emission at night, which requires the excitation of the upper states of these lines ( $^2P_{1/2}$  and  $^2P_{3/2}$ ) by chemical reactions. The chemiluminescent Na(D) lines discovered by Slipher (1929) are among the most prominent emissions of the optical nightglow spectrum (Cosby et al., 2006; Noll et al., 2012; Osterbrock et al., 1996) and have therefore been the topic of various studies (e.g., Chapman, 1939; Plane et al., 2012; Slanger et al., 2005; von Savigny et al., 2016). In contrast, determination of the nocturnal  $K(D_1)$  emission was not successful for a long time. Swider (1987) suggested that K nightglow is mostly produced by a process analogous to that proposed by Chapman (1939) for the Na(D) emission, which would therefore comprise the reactions



and



where  $K(^2P_J)$  can be produced in one of two spin-orbit multiplets ( $J = 1/2, 3/2$ ). The propensity for producing  $J = 3/2$  rather than  $J = 1/2$ , which is controlled by the symmetries of the molecular orbitals involved (Plane et al., 2012), then governs the relative intensities of the  $D_2$  to the  $D_1$  emission lines. Swider (1987) noted that KO in reaction (4) is also created by the reaction sequence



with a contribution of around 20%. Considering all nightglow-relevant processes, Swider (1987) estimated a  $K(D_1)$  intensity of about 0.5 R (Rayleigh), which was too faint to be detected in those days. With the advent of astronomical telescopes of the 10-m class and powerful high-resolution echelle spectrographs, the situation changed. Osterbrock et al. (1996) released an atlas of night-sky emission lines based on observations with the High-Resolution Echelle Spectrometer (HIRES) at the Keck I telescope on Mauna Kea (Hawaii, 20°N, 155°W). With an exposure time of 60 min and a resolution of 0.02 nm, the spectrum showed a weak line which could be  $K(D_1)$ . However, Osterbrock et al. (1996) were skeptical since they did not detect the  $K(D_2)$  line, unaware of its strong atmospheric absorption.  $K(D_1)$  was then clearly identified by Slanger and Osterbrock (2000), who benefitted from a much larger HIRES data set with a total exposure time of about 100 hr at the line wavelength. Slanger and Osterbrock (2000) measured a mean intensity of 1.0 R, which is about 20 times weaker than the also measured Na( $D_1$ ) line and of the same order as the estimate of Swider (1987). Finally, Hanuschik (2003) produced a line atlas based on night-sky spectra of the Ultraviolet and Visual Echelle Spectrograph (UVES) at the Very Large Telescope at Cerro Paranal in Chile (24.6°S, 70.4°W).

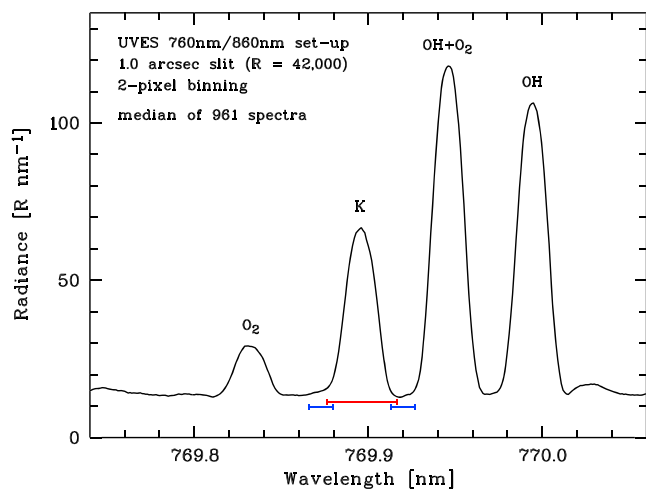


**Figure 1.** Measurement of the  $K(D_1)$  line. The plotted spectrum is the median of 961 spectra taken with Ultraviolet and Visual Echelle Spectrograph (UVES) setups with central wavelengths of 760 or 860 nm, the standard slit width of  $1.0''$ , and two-pixel binning. For the selected slit width, the plot shows the wavelength ranges for the line integration (red) and the continuum determination (blue).  $K(D_1)$  at 769.90 nm in air and nearby lines from the R-branch of  $O_2(b-X)(1-1)$  and the P-branch of  $OH(4-0)$  are labeled.

With a total exposure time of 9 hr and a resolving power of 43,000 (slightly higher than for the HIRES data) at the position of  $K(D_1)$  in the spectrum, Cosby et al. (2006) also identified this line at the expected strength.

So far, only the typical intensity of the  $K(D_1)$  line is known. Nocturnal, seasonal, and long-term variability have not been investigated. Moreover, a detailed comparison to an atmospheric model including state-of-the-art K chemistry has not been undertaken. This would be promising with respect to a better understanding of these chemical processes and the related dynamics. Furthermore, because  $K(D_2)$  cannot be observed, recent advances in understanding the molecular dynamics of these chemiluminescent reactions can be used to predict the total  $K(D)$  emission. Finally, it is desirable to determine the overall quantum yield, that is, efficiency of reaction (3) of K with ozone and reaction (4) of KO with atomic oxygen with respect to the production of  $K(D)$  nightglow photons. In the present study, we have performed such an investigation based on a large set of high-resolution UVES spectra described by Noll et al. (2017), a Whole Atmosphere Community Climate Model (WACCM) including the K chemistry developed by Plane et al. (2014), satellite-based K density data retrieved from OSIRIS (Dawkins et al., 2014, 2015), and different atmospheric properties from the Sounding of the Atmosphere using Broadband Emission Radiometry (SABER) instrument onboard the Thermosphere Ionosphere Mesosphere Energetics Dynamics satellite (Mlynczak et al., 2018; Russell et al., 1999). The discussion of the results will also include comparisons to the much better studied  $Na(D)$

nightglow, where data related to Cerro Paranal were analyzed by Unterguggenberger et al. (2017). Such comparisons will be valuable for an improved understanding of similarities and differences in the physical and chemical properties of two alkali metals primarily differing in mass and size.

This paper is structured as follows. First, we will introduce the UVES data set for  $K(D_1)$  including the description of the intensity measurements (section 2). The UVES-based results on the  $K(D_1)$  variations will be discussed in section 3. Theoretical predictions of the intensity of the unobserved  $K(D_2)$  relative to the measured  $K(D_1)$  line will be made in section 4. The WACCM model including K chemistry and the resulting K nightglow variations will be described in section 5. Then, we will use satellite-based data for the different ingredients of the K nightglow chemistry to evaluate the UVES- and WACCM-based climatologies and to estimate the total quantum yield of K nightglow (section 6). Finally, we will draw our conclusions in section 7.

## 2. UVES Data Set

The Very Large Telescope spectrograph UVES (Dekker et al., 2000) is an optical high-resolution echelle spectrograph, which covers a wavelength range of several hundred nanometers by the simultaneous observation of various spectral orders. The  $K(D_1)$  line is covered by two spectral setups with central wavelengths of 760 and 860 nm. The spectral resolving power mostly varies between 21,000 and 107,000, which corresponds to angular widths of the entrance slit between  $2.0''$  and  $0.3''$ . The slit lengths are either  $8''$  for the 760 nm or  $12''$  for the 860-nm setup. Despite the very small solid angle covered, high signal-to-noise ratios (S/N) can be achieved due to a diameter of 8 m of the telescope's primary mirror.

The European Southern Observatory provides the UVES data as so-called Phase 3 products, which include one-dimensional spectra of the astronomical targets and the night-sky background emission. For a study of hydroxyl (OH) nightglow, Noll et al. (2017) selected about 10,400 archived night-sky spectra for the two setups taken between April 2000 (start of the archive) and March 2015. The data had to be postprocessed for an accurate flux calibration. The complex procedure is described in detail by Noll et al. (2017). The resulting absolute flux calibration accuracy is 5% to 10%.

Figure 1 shows a median spectrum of the  $K(D_1)$  wavelength region based on 961 spectra taken with the standard  $1.0''$  slit (corresponding to a resolving power of 42,000) and two-pixel binning. The exact location of the  $K(D_1)$  line was taken from the database of the National Institute of Standards and Technology for

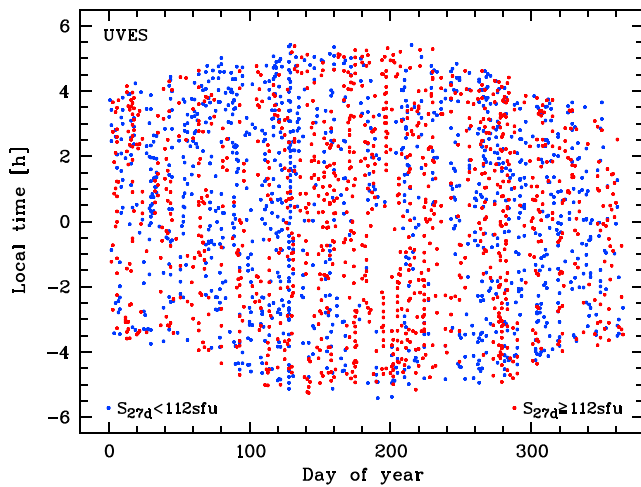


**Figure 2.** Sample of 2,299 Ultraviolet and Visual Echelle Spectrograph (UVES) spectra used for this study. The local time of the midexposure and the local day of year are shown for observations with low (blue) and high (red) solar activity. The sample was split at the median solar radio flux of 112 sfu, which was averaged for 27 days ( $S_{27d}$ ) and centered on the day of observation.

atomic data. The wavelength of 769.8965 nm in air based on laboratory experiments (Sansonetti, 2008) agrees well with the line peak in Figure 1, which is at 769.896 nm. The plotted spectrum illustrates that  $K(D_1)$  is in a crowded region with nearby lines from the R-branch of  $O_2(b-X)(1-1)$  and the P-branch of  $OH(4-0)$  (see also Slanger & Osterbrock, 2000). For this reason,  $K(D_1)$  can only be studied if the spectral resolution is sufficiently high. Hence, we only considered spectra with a resolving power of more than 34,000. This limitation only reduces the data set by 3%. A more restrictive selection criterion is the exposure time, which was between 1 and 135 min. We have chosen a minimum value of 10 min in order to make sure that the S/N is sufficiently high for a reliable intensity measurement. Forty-one percent of the spectra fulfill this criterion.

Figure 1 illustrates the line measurement for the standard slit. The most robust results were obtained for a line integration range with a width of 0.04 nm. Before the integration, a constant continuum was subtracted. It was derived as the mean of the median values in two continuum windows with a width of 0.015 nm, which enclose the  $K(D_1)$  line. There is a small overlap of each continuum window with the integration range of 0.005 nm. This improves the quality of the continuum and line intensity without causing a significant contamination of the continuum by the line. For spectra with a different resolution, the integration range and the continuum windows inside this interval were scaled linearly. Only the outer

limits of the continuum ranges remained unchanged. They were always 0.06 nm apart in order to minimize the influence of the slit width on the line measurement. The differences in the median values of both continuum windows combined with the standard deviation for the pixels in both windows in quadrature were used to derive the uncertainty in the continuum level and the corresponding line intensity.

Continuum levels derived for a wider wavelength range of 0.5 nm in width were also used for the sample selection. Only spectra with continuum brightnesses between 2 and 100 R/nm were kept. This corresponds to 3,146 line measurements or 76% of the previous sample. In particular, the upper limit is important in order to avoid spectra with strong contaminations of the continuum by the astronomical target. Contaminations cannot fully be avoided as the entrance slit is relatively short and the astronomical objects observed with UVES are often quite bright. For this reason, the remaining 3,146 spectra were checked by eye to identify extraterrestrial features like absorption or emission lines affecting the continuum derivation or line integration. In this context, it has to be known that certain stars can show strong K absorption. Their impact on our  $K(D_1)$  measurements depends on the Doppler shift due to their radial velocity relative to the Earth. Eventually, 2,302 (73%) reliable line measurements were identified. As three of them are related to 2015, which is not covered by the WACCM simulation described in section 5 (due to the limitation of the available input), it makes sense to only consider the 2,299 spectra taken between April 2000 and December 2014.

Figure 2 shows the temporal distribution of the final sample in terms of local time (LT) and day of year. The data set is well suited to derive a climatology (see section 3.1) as the nocturnal periods are well covered all over the year. The minimum solar zenith angle is  $104^\circ$  at midexposure and above  $101^\circ$  for the entire exposure, which is large enough to exclude fluorescence (section 1) as an emission process for  $K(D_1)$  due to terminator heights of the Earth's shadow well above 100 km for all spectra. Figure 2 also shows the temporal distribution for subsamples related to low and high solar activity, which is interesting for the discussion of long-term variations in section 3.2. The sample was split in groups of equal size at a 10.7-cm solar radio flux (Tapping, 2013) of 112 solar flux units (sfu) for an averaging period of 27 days ( $S_{27d}$ ) characterizing the solar rotation (cf. Noll et al., 2018). Both subsamples show a good time coverage, although the data for low solar activity seem to display a patchier distribution. The areas lacking any data appear to be small enough to be noncritical for the analysis of long-term variations. The distribution of observing dates over the different years is also relatively smooth (cf. Noll et al., 2017). The median observing date was in March 2007.

The spectra in our UVES sample originate from astronomical observations toward various lines of sight. The zenith angles ranged from  $1^\circ$  to  $69^\circ$  with a mean value of  $36^\circ$ . First, this results in different geographical locations at the altitude of the  $K(D_1)$  emission layer. The mean and maximum horizontal distances

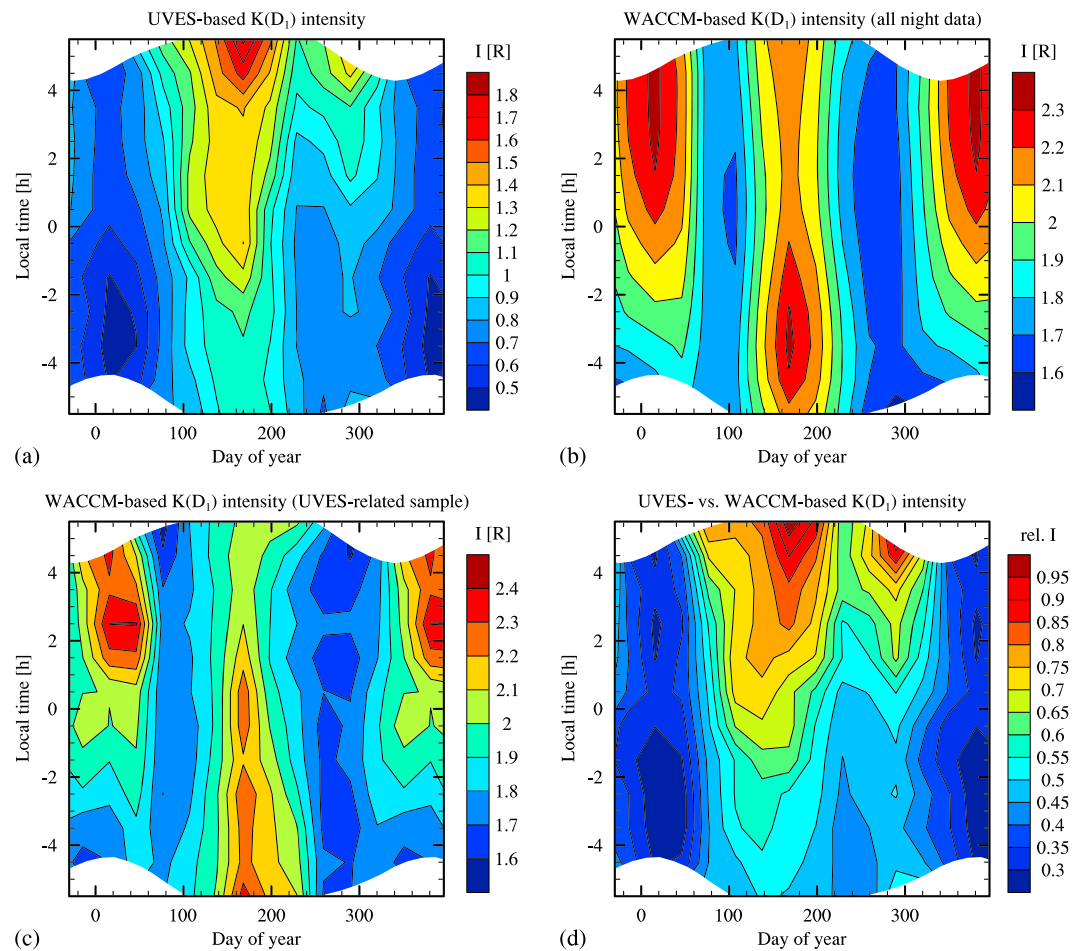


**Figure 3.** Contour plots of measured and modeled  $K(D_1)$  intensities at Cerro Paranal in Rayleighs for a  $12 \times 12$  grid of local times in hours and days of year. The contours are only shown for nighttime conditions with solar zenith angles larger than  $100^\circ$ . The displayed climatologies for Cerro Paranal are based on line measurements in 2,299 Ultraviolet and Visual Echelle Spectrograph (UVES) spectra (a), nighttime line intensities from 115,080 time steps of a Whole Atmosphere Community Climate Model (WACCM) simulation for a quantum yield of 100% with respect to  $KO + O$  and a fixed D-line ratio  $R_D$  of 1.67 (section 5) (b), and only those time steps of the WACCM simulation best matching the UVES data (c). Finally, (d) shows a contour plot for the ratio of the observed and modeled K nightglow intensities from (a) and (c).

are about 70 and 220 km, respectively (cf. Noll et al., 2017). Second, the projected width of the  $K(D_1)$  emission layer varies. Therefore, all measured intensities were corrected for the van Rhijn effect (van Rhijn, 1921); that is, the intensities are representative of the zenith under the assumption of a horizontally homogeneous layer with an altitude of 90 km. Similar to Noll et al. (2015) and Noll et al. (2017), we also corrected the line intensities for molecular absorption in the atmosphere by combining calculations with the Line-By-Line Radiative Transfer Model (Clough et al., 2005) for input profiles representative of Cerro Paranal and Doppler-broadened emission line profiles for a temperature of 190 K. These calculations show that  $K(D_1)$  is hardly affected by absorption. Toward the zenith, the atmospheric transparency is 99.8%. In contrast, the corresponding transmission for  $K(D_2)$  is only 0.3%, which confirms that this line cannot be observed from the ground due to its almost complete absorption by the  $O_2$  A-band.

### 3. Variability of K Nightglow

With 2,299 individual line measurements, the variability of the  $K(D_1)$  intensity  $I_{K(D_1)}$  can be studied for the first time. The sample indicates strong variations at about  $25^\circ S$  and  $70^\circ W$  over the whole period from 2000 to 2014. The intensities range from 0.2 to 4.8 R with a standard deviation of 0.6 R. This result is quite robust

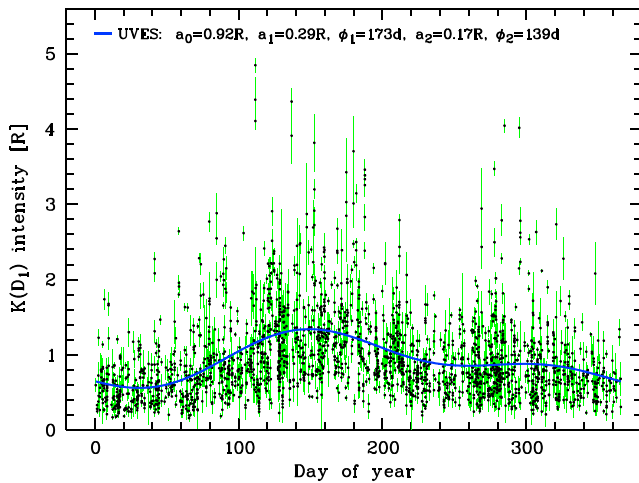


**Figure 4.** Seasonal variations of  $K(D_1)$  intensity in Rayleighs for a sample of 2,299 Ultraviolet and Visual Echelle Spectrograph (UVES) spectra. The individual data points are provided with error bars which reflect the line measurement uncertainties (neglecting the general flux calibration uncertainty of 5% to 10%). The plot also shows the results of a harmonic analysis of the intra-annual variations (best fit curve and its coefficients).

since 94% of the  $K(D_1)$  line measurements were at least  $3\sigma$  detections with respect to the uncertainty in the line intensity, which was 0.11 R on average. Only 28 measurements mostly related to faint lines showed confidence levels below  $2\sigma$ . The mean intensity of the sample is 0.95 R. As statistical uncertainties can be neglected due to the large sample size and the relatively small individual errors, the uncertainty of the mean value is mainly determined by the quality of the absolute flux calibration (see section 2). The latter results in an uncertainty of 0.05 to 0.10 R. Hence, our mean value is in excellent agreement with the 1.0 R derived by Slanger and Osterbrock (2000) based on 100 hr of data taken at Mauna Kea between 1993 and 1997 (Osterbrock et al., 1998, 2000). This result suggests that the differences in the observing site and covered time period do not significantly affect the mean  $I_{K(D_1)}$ . As indicated by the global K density distribution (Dawkins et al., 2015), this cannot necessarily be expected, especially for large latitude differences.

### 3.1. Climatology

The good time coverage of our UVES sample shown in Figure 2 allows us to derive a climatology of the  $I_{K(D_1)}$  variations with respect to LT and day of year. In the same way as described in Noll et al. (2017, 2018), we built a  $12 \times 12$  climatological grid with points at the centers of the LT hours between 18:00 and 6:00 and the central days of the 12 months.  $I_{K(D_1)}$  for each grid point was calculated by weighted averaging of the intensities of

the individual measurements based on the temporal difference between the individual data points and the grid point using two-dimensional Gaussians with  $\sigma$  of half an hour and half a month as weights.

The resulting climatology is shown in Figure 3a. The contours are only given for solar zenith angles of at least  $100^\circ$ , that is, nighttime conditions. There is an interesting variability pattern with the strongest emissions in the middle of the year and toward the end of the night. The maximum of about 1.9 R is in June. In addition, there is a secondary maximum with about 1.3 R in October, which is also located in the morning hours. The minimum intensities of about 0.5 R are found in the first hours of the night in January. The weakest and strongest nocturnal variations are present in December and June with maximum-minimum differences of about 0.2 and 0.8 R, respectively.

For a more quantitative evaluation of the seasonal variations, we performed a harmonic analysis in the same way as described in Noll et al. (2018). The constant  $a_0$ , the amplitude  $a_1$  and phase  $\phi_1$  of the AO, and the amplitude  $a_2$  and phase  $\phi_2$  of the SAO were taken from the fit function

$$f(t) = a_0 + a_1 \cos\left(\frac{2\pi(t - \phi_1)}{n}\right) + a_2 \cos\left(\frac{4\pi(t - \phi_2)}{n}\right), \quad (7)$$

where  $n$  equals 365.25 and  $t$  is the time coordinate in days.

Figure 4 shows the individual  $K(D_1)$  intensities with their uncertainties and the resulting fit curve based on equation (7) as a function of the day of year. The resulting AO and SAO coefficients are also listed in Table 1. The AO with a relative amplitude of 31% clearly dominates the seasonal variations. It is almost twice as large as the 18% for the SAO. This result is robust as the uncertainty is only 2% in both cases. The maximum in early southern winter is further strengthened by the small difference in the phases  $\phi_1$  (June) and  $\phi_2$  (May) of only 34 days (with an uncertainty of a few days), which results in a 46% higher intensity at the maximum than for  $a_0$ . In contrast, the secondary maximum in October is very shallow due to the negative interference of AO and SAO. The minimum of the fit curve in southern summer is 39% lower than  $a_0$ . As indicated in Table 1, we also performed the harmonic analysis for the monthly intensities of the climatological grid, which correspond to averages of the hourly values weighted for the time fraction of each hour with a solar zenith angle above  $100^\circ$ . Based on the 12 monthly intensities, the resulting coefficients of the harmonic analysis are very similar to those for the individual measurements. The values are consistent within the small errors. The good agreement confirms the good time coverage of the UVES data set. We also checked how the AO and SAO coefficients change for a separate analysis of the seasonal variations for each hour in the climatological grid. While  $a_0$  increases by 42% from 19:30 to 4:30 LT, there is no clear trend for

**Table 1**  
*Harmonic Analysis of Seasonal Variations of the Measured  $K(D_1)$ , Simulated  $K(D_1)$ , and Measured  $Na(D)$  Intensity at Cerro Paranal<sup>a</sup>*

Line(s)	Origin	$N$	$a_0$ (R)	$a_1/a_0$	$\phi_1$ (d)	$a_2/a_0$	$\phi_2$ (d)
$K(D_1)$	UVES	2,299	0.921 (0.011)	0.311 (0.017)	173 (3)	0.182 (0.016)	139 (3)
		12 <sup>b</sup>	0.917 (0.015)	0.310 (0.024)	172 (4)	0.157 (0.024)	138 (4)
		2,299 <sup>c</sup>	1.912 (0.011)	0.039 (0.007)	92 (12)	0.122 (0.008)	1 (2)
$K(D_1)$	WACCM	115,080	1.919 (0.002)	0.044 (0.001)	93 (2)	0.148 (0.001)	182 (0)
		12 <sup>b</sup>	1.902 (0.023)	0.042 (0.017)	112 (24)	0.102 (0.017)	3 (5)
		115,080	1.919 (0.002)	0.044 (0.001)	93 (2)	0.148 (0.001)	182 (0)
$K(D_1)$	WACCM	115,080	1.919 (0.002)	0.044 (0.001)	93 (2)	0.148 (0.001)	182 (0)
		12 <sup>b</sup>	1.920 (0.020)	0.043 (0.015)	95 (20)	0.128 (0.015)	183 (3)
		115,080	1.919 (0.002)	0.044 (0.001)	93 (2)	0.148 (0.001)	182 (0)
$Na(D)$	X-shooter <sup>d</sup>	3,662	39.9 (1.1)	0.25 (0.01)	191 (8)	0.30 (0.06)	108 (1)

<sup>a</sup>Uncertainties are given in parentheses. <sup>b</sup>Monthly nighttime averages from climatological grid. <sup>c</sup>In best temporal agreement with the UVES data. <sup>d</sup>From Unterguggenberger et al. (2017).

the amplitudes relative to  $a_0$  and phases of AO and SAO. Therefore, the night-averaged results shown in Table 1 well describe the seasonal variations independent of the time. This is very different from the situation for OH analyzed by Noll et al. (2018) also using UVES data, where especially  $a_1$  strongly decreases in the night-averaged seasonal variations due to large  $\phi_1$  changes in the course of the night.

In terms of the underlying chemistry, the Na(D) nightglow is the most interesting emission for comparison with our  $K(D_1)$  measurements. The Na(D) variability at Cerro Paranal was studied by Unterguggenberger et al. (2017) based on 3,662 spectra from the X-shooter echelle spectrograph taken between October 2009 and March 2013. The corresponding results for the harmonic analysis of the sum of the  $D_1$  and  $D_2$  intensities are also provided in Table 1. Despite Na and K being elements in Group 1 of the periodic table and thus with chemistries which would be expected to be similar, the seasonal nightglow variations are very different. With amplitudes of  $a_1$  and  $a_2$  of about 25% and 30% relative to  $a_0$  and phases  $\phi_1$  and  $\phi_2$  in July and April/October, there is a clear SAO with similar maxima around the equinoxes and a main minimum in January. As already discussed in section 1, the abundances of Na and K also show significant differences in their seasonal variability. Plane et al. (2014) explained this by temperature-dependent differences in the production of Na/K by the destruction of  $NaHCO_3/KHCO_3$  as well as  $Na^+/K^+$  clusters. This will certainly contribute to the contrasting behavior in the intra-annual nightglow variations. Chemistry could also affect the nocturnal variability, which also differs for  $K(D_1)$  and Na(D). Unterguggenberger et al. (2017) found clear changes in the nocturnal variability pattern depending on season. Except for southern spring, there is no significant intensity increase from the evening to the morning as it is observed for  $K(D_1)$  emission during the entire year. Note that a part of the differences in the variability could be caused by the fact that we could not measure the  $K(D_2)$  line. The ratio of the  $D_2$  and  $D_1$  intensity  $R_D$  of Na varies between 1.2 and 1.8 (Slanger et al., 2005) or 1.5 and 2.0 (Plane et al., 2012). According to laboratory experiments (Slanger et al., 2005), the variation is correlated with the concentration ratio for O and  $O_2$ . The  $R_D$  for K will be discussed in section 4.

### 3.2. Long-Term Variations

With a time coverage of almost 15 years, our  $I_{K(D_1)}$  time series is sufficiently long for a study of the impact of the solar activity cycle of about 11 years. A possible linear long-term trend should be considered as an additional source of uncertainty. In the same way as described by Noll et al. (2017) for the UVES-related OH nightglow observations, solar cycle effect  $a_{SC}$  and trend  $a_T$  were derived by a bilinear regression analysis using

$$f(t) = a_0 + a_{SC}S_{27d} + a_T t \quad (8)$$

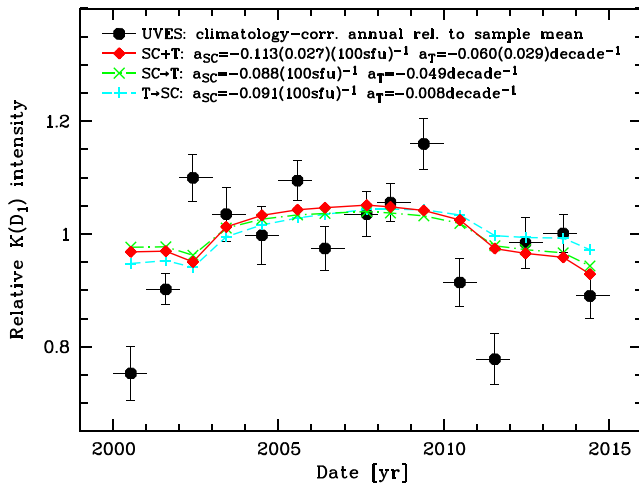


**Figure 5.** Long-term variations of Ultraviolet and Visual Echelle Spectrograph (UVES)-based  $K(D_1)$  intensities relative to the sample mean. The filled circles and their error bars show the annual averages and mean errors for the years from 2000 to 2014 plotted for the corresponding mean date in years. The horizontal bars mark the duration of each year. The plot also displays results of a regression analysis for a linear solar cycle effect using  $S_{27d}$  and a possible linear long-term trend based on the 2,299 individual intensity measurements. The solid lines with filled diamonds show the simultaneous bilinear fit, whereas dash-dotted lines with  $\times$  symbols and dashed lines with  $+$  symbols indicate consecutive fits of both effects starting with solar forcing and long-term trend, respectively. The listed relative fit coefficients  $a_{SC}$  and  $a_T$  are provided per 100 sfu and per decade. For the simultaneous fit, uncertainties based on regression errors and flux calibration uncertainties are also shown.

in  $-9.1\%$  per 100 sfu. These percentages are in good agreement with the results for the simultaneous fit. Moreover, the fit curves for the three cases in Figure 5 are very similar, which confirms that possible linear trends are not an issue for the derivation of the solar cycle effect. For such a robust result, it was certainly important to cover two solar activity maxima. Of course, the quality of the findings depends on the assumption that the relation has only linear terms and that both effects do not influence each other; that is,  $a_{SC}$  is not time dependent.

A solar cycle effect with a negative sign is in contrast to other airglow emissions that were measured at Cerro Paranal. For a similar UVES sample, Noll et al. (2017) found  $+16.1 \pm 1.9\%$  per 100 sfu and no significant long-term trend for different OH bands on average. Noll et al. (2012) investigated emissions from O, O<sub>2</sub>, OH, and Na based on more than 1,000 FORS 1 low-resolution spectra taken between April 1999 and February 2005. For Na(D) the resulting effect was about  $+11\%$  per 100 sfu, that is, the same amount but the opposite sign. This result was obtained without fitting a long-term trend. We will further discuss the long-term  $I_{K(D_1)}$  variations by means of model comparisons in section 5.2.

#### 4. Theoretical Predictions for $K(D_2)$

As the  $K(D_2)$  line is almost completely absorbed in the Earth's atmosphere (section 2) and even not accessible from space as it is swamped by the bright O<sub>2</sub> A-band emission (Dawkins et al., 2014), its intensity relative to  $K(D_1)$ , that is,  $R_D$ , needs to be estimated by theoretical considerations.

Reaction (3) between K and O<sub>3</sub> and reactions (5) and (6) involving KO<sub>2</sub> lead to the formation of KO. The ground and the first excited electronic states of this molecule are  $^2\Sigma$  and  $^2\Pi$ , respectively (Lee et al., 2002; Vasiliu et al., 2010). The latter splits into  $^2\Pi_{3/2}$  and  $^2\Pi_{1/2}$  states because of spin-orbit coupling with the ground state (Lee et al., 2002). As the  $^2\Pi_{3/2}$  state is only 2.1 kJ/mol higher in energy than  $^2\Sigma_{1/2}$  (Lee et al., 2002; Vasiliu et al., 2010), there will be a significant thermal population of  $KO(^2\Pi_{3/2})$  at mesospheric temperatures (e.g., 19% at 200 K). This is quite different from the case of NaO, where NaO( $^2\Pi$ ) is the ground state and

with  $S_{27d}$  (section 2) as the proxy for the solar cycle effect. In a preparatory step, we corrected possible biases due to year-dependent time gap distributions in the UVES data set. For this, the climatological variations shown in Figure 3a were removed from the time series by subtracting the difference between the intensity at the closest grid point and the climatology-based annual mean for each  $K(D_1)$  measurement. It turned out that the changes in the result are smaller than the uncertainties of the regression analysis. We also investigated the impact of the quality of the absolute flux calibration on the regression results, which matters since the UVES products originate from different instrumental setups and were processed with different calibration data depending on the year of observation (Noll et al., 2017). The calculations show that typical relative flux calibration errors of about 2% result in uncertainties in the solar cycle effect and long-term trend that are about 1 order of magnitude smaller than those from the regression analysis, which therefore dominate the error budget.

As shown in Figure 5, we find a solar cycle effect of  $-11.3 \pm 2.7\%$  per 100 sfu and a long-term trend of  $-6.0 \pm 2.9\%$  per decade for  $I_{K(D_1)}$  relative to the sample mean at Cerro Paranal between 2000 and 2014. For the trend, the uncertainties are too high for a safe  $3\sigma$  detection, as expected. The solar cycle effect is clearly negative. Although the year-to-year variations of the relative annual mean intensity shown in Figure 5 are relatively high (partly due to subsample sizes of only 64 to 274), the annual mean values support this result as they tend to be higher in the middle of the period, that is, during low solar activity. In order to better understand the influence of the uncertain long-term trend on the solar cycle effect, we also performed consecutive fits of both linear terms in equation (8). For a fit of  $a_{SC}$  without long-term trend, we obtain  $-8.8\%$  per 100 sfu, whereas the primary fit of  $a_T$  and the subsequent derivation of the solar forcing results



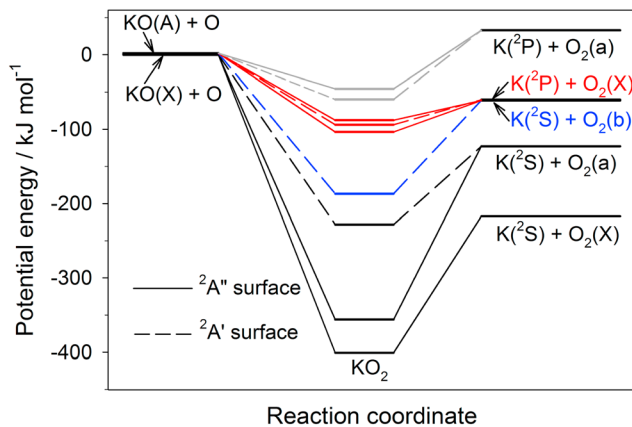


**Figure 6.** Correlation diagram for the electronic potential energy surfaces connecting the reactants  $\text{KO}(X^2\Sigma) + \text{O}$  and  $\text{KO}(A^2\Pi) + \text{O}$  with the products  $\text{K} + \text{O}_2$  through the  $\text{KO}_2$  intermediate. The  $\text{KO}_2$  excited state energies are calculated at the TD/B3LYP/6-311+g(2d,p) level of theory. Quartet surfaces have been omitted (for clarity) since these are highly repulsive states, which do not influence the electronic nature of the products. Surfaces colored red produce  $\text{K}(^2\text{P})$  and thus contribute to the K nightglow emission. The blue surface produces  $\text{K} + \text{O}_2(b^1\Sigma_g^+)$ . Surfaces colored gray are endothermic channels, which are not reactive at mesospheric temperatures.

$\text{NaO}(A^2\Sigma)$  is about 21 kJ/mol higher in energy, so that the reaction dynamics of the two states need to be treated separately, including the effect of quenching of  $\text{NaO}(A^2\Sigma)$  by  $\text{O}_2$  (Plane et al., 2012).

The reactions of  $\text{KO}(X^2\Sigma)$  and  $\text{KO}(A^2\Pi)$  with  $\text{O}(^3\text{P})$  to form  $\text{K} + \text{O}_2$  occur on electronic surfaces of  $C_s$  symmetry (the only symmetry element is the plane containing the three atoms) with doublet spin multiplicity (the quartet surfaces are strongly repulsive).  $\text{KO}(X^2\Sigma) + \text{O}(^3\text{P})$  occurs on three electronic surfaces (one of  $^2A'$  symmetry and two of  $^2A''$  symmetry) and  $\text{KO}(A^2\Pi) + \text{O}(^3\text{P})$  occurs on six doublet electronic surfaces (three of  $^2A'$  and three of  $^2A''$  symmetry; Huber & Herzberg, 1979). However, because of an avoided crossing between the  $^2\Sigma_{1/2}$  and  $^2\Pi_{1/2}$  states of  $\text{KO}$ , the  $^2\Pi_{1/2}$  state is 6.5 kJ/mol above the  $^2\Sigma_{1/2}$  ground state (Lee et al., 2002). Thus, at mesospheric temperatures only around 1% of the  $\text{KO}$  molecules will be in the  $^2\Pi_{1/2}$  state (assuming it is thermalized, which is likely given that  $\text{KO}$  will undergo about 500 collisions with  $\text{N}_2$  and  $\text{O}_2$  before colliding with an  $\text{O}$  atom). When  $\text{KO}(X^2\Sigma_{1/2}$  or  $A^2\Pi_{3/2})$  interacts with  $\text{O}$ , there are likely to be six reactive surfaces, of which three lead to  $\text{K}(^2\text{P})$  and production of a photon. That is, purely statistical considerations would suggest a quantum yield of 50% (cf. section 6.2). As in Plane et al. (2012) for the Na nightglow, the ion-pair  $\text{K}^+\text{O}_2^-$  states need to be considered since these are the last intermediates before formation of the reaction products and hence are likely to determine the spin-orbit state of the  $\text{K}(^2\text{P}_J)$  product and  $R_D$ .

Figure 6 illustrates the resulting correlation diagram between reactants and products. The reaction between  $\text{KO}$  and  $\text{O}$  is sufficiently exothermic (by 217 kJ/mol adopting a  $\text{K}-\text{O}$  bond energy of 274 kJ/mol; Vasiliu et al., 2010) to produce  $\text{K}(^2\text{S})$  and  $\text{O}_2(X^3\Sigma_g^-)$ ,  $\text{O}_2(a^1\Delta_g)$ , or  $\text{O}_2(b^1\Sigma_g^+)$ , as well as  $\text{K}(^2\text{P})$  and  $\text{O}_2(X^3\Sigma_g^-)$  or  $\text{O}_2(a^1\Delta_g)$ . The energies of the  $\text{K}^+\text{O}_2^-$  intermediate states are calculated by optimizing the geometry of each excited state using the time-dependent hybrid density function/Hartree-Fock (TD/B3LYP) method with the 6-311+g(2d,p) basis set from within the Gaussian suite of programs (Frisch et al., 2016).

Figure 6 shows that there are eight excited states of  $\text{KO}_2$  which are all below the energies of the entrance channel  $\text{KO}(X \text{ or } A) + \text{O}$ , and so there should be no potential energy barriers on the nine surfaces including the  $\text{KO}_2$  ground state surface. However, the product  $\text{K}(^2\text{P}) + \text{O}_2(a^1\Delta_g)$  is 33-kJ/mol endothermic and thus inaccessible at mesospheric temperatures (the two surfaces connecting this product state are depicted with gray lines in Figure 6). This leaves seven reactive surfaces. Of these, three surfaces (one  $^2A'$  and two  $^2A''$  surfaces, shown with red lines in Figure 6) connect to  $\text{K}(^2\text{P}) + \text{O}_2(X)$ , hence producing nightglow emission. As discussed in Plane et al. (2012), orbital symmetry considerations indicate that reaction on a  $^2A'$  surface has a statistical  $J = 3/2$  to  $1/2$  propensity of 1, while reaction on a  $^2A''$  surface has a statistical  $J = 3/2$  to  $1/2$  propensity of 2. Thus, the averaged spin-orbit propensity for the three surfaces producing  $\text{K}(^2\text{P})$  is  $(1 + 2 + 2) / 3 = 1.67$ . That is, given the mixing of the  $\text{KO}(X)$  and  $\text{KO}(A)$  states (see above) and assuming an equal probability of reaction on each of these three surfaces,  $R_D$  should be 1.67. Considering the mean  $\text{K}(D_1)$  intensity of 0.95 R from section 3, this ratio would result in a mean intensity of the  $\text{K}(D_2)$  emission of about 1.6 R at Cerro Paranal. The corresponding total emission of the  $\text{K}(D)$  doublet would then be about 2.5 R.

## 5. K Nightglow Simulation With the WACCM-K Model

WACCM-K is a global model of the meteoric K layer (Plane et al., 2014), which was developed by adding a module of neutral and ion-molecule potassium chemistry, together with a meteoric input function of  $\text{K}$ , into WACCM (Garcia et al., 2007; Marsh et al., 2013). WACCM-K simulations of the seasonal and diurnal variations of the K layer compare well with lidar observations at several latitudes (Feng et al., 2015; Plane et al., 2014), as well as near-global observations by satellite-borne observations of K resonance fluorescence in the dayglow (Dawkins et al., 2015). For the present study, we employed a specified dynamics version of WACCM4, where the model was nudged with the reanalysis winds and temperatures from National Aeronautics and Space Administration's Modern-Era Retrospective Analysis for Research and Applications

(Lamarque et al., 2012) below 60 km. WACCM4 uses the framework from the fully coupled Community Earth System Model (CESM version 1, e.g., Hurrell et al., 2013), which includes the detailed physical processes in the Community Atmosphere Model, version 4 (CAM4; Neale et al., 2012) and the fully interactive chemistry described in Kinnison et al. (2007). The model has a horizontal resolution of  $1.9^\circ$  latitude  $\times$   $2.5^\circ$  longitude and 88 vertical model levels from the surface up to about 140 km, which results in a height resolution of about 3.5 km in the upper mesosphere. The model was initialized with output from an earlier WACCM-K run (Plane et al., 2014) and was then run from 2000 to 2014. The global fields were saved daily and the output at the location of Cerro Paranal was sampled every 30 min.

The intensities of the K nightglow used in this section were derived from reaction (4) between KO and atomic oxygen under the assumption that each resulting K atom leads to the emission of a photon; that is, the retrieved vertically integrated emission  $I_{K(D)}$  represents both K(D) lines for a quantum yield of 100%. For the discussion of the quantum yield in section 6.2, we also calculated K(D) intensities only considering the rate of production of KO molecules from reaction (3) between K and ozone and excluding the rate of production from the alternative pathway involving  $KO_2$  (see reactions (5) and (6) in section 1). For a comparison with the UVES-based results for  $K(D_1)$ , we divide the WACCM-related intensities by a factor of 2.67, that is,  $1 + R_D$  as estimated in section 4. The use of a fixed  $R_D$  does not consider possible variations as those related to Na (see section 3.1). However, they should be negligible in comparison to other influences as the energy differences between KO(A) and KO(X) (section 4) are much smaller than those for NaO(A) and NaO(X) (Plane et al., 2012).

### 5.1. Climatology

In the same way as for the UVES data in section 3.1, we can derive a climatology for  $I_{K(D_1)}$  variations from WACCM. For this purpose, we consider all simulation results for Cerro Paranal between 2000 and 2014 with solar zenith angles of at least  $100^\circ$ , that is, nighttime conditions as met by the UVES data. In total, there are 115,080 selected time steps. The result is shown in Figure 3b. The climatology is quite different from the UVES observations displayed in Figure 3a. Instead of a dominating AO with a peak in the middle of the year, the WACCM results show a prevailing SAO. The differences in the seasonal variations can be quantified by a harmonic analysis as described in section 3.1. Table 1 shows its results for the individual and the gridded data, which agree well with each other. For the former, we find relative amplitudes of the AO and SAO of about 4% and 15%, respectively. This corresponds to a ratio of  $a_2$  to  $a_1$  of  $3.37 \pm 0.09$ , which is distinctly higher than  $0.59 \pm 0.06$  for the UVES data. This difference is mostly caused by the much weaker  $a_1$  for WACCM (4 vs. 31%), whereas  $a_2$  is relatively similar (15 vs. 18%). There is also no agreement with respect to the phases  $\phi_1$  (93 vs. 173 days) and  $\phi_2$  (182 vs. 139 days). Nevertheless, the K nightglow intensity peaks in June for both data sets. The main difference is the additional WACCM-related strong maximum in January and the missing weak maximum in October. Clear discrepancies are also found for the nocturnal variations. In particular for the maximum in June, there are oppositional nocturnal trends. While the UVES-based  $K(D_1)$  intensities for June in Figure 3a increase by about 68% from the evening to the morning, there is a weak decrease of 6% between 20:30 and 5:30 LT for WACCM in Figure 3b. The situation is distinctly better for January, where both data sets show an increase of 31% from dusk till dawn.

A reason for the discrepancies between the UVES- and WACCM-based climatologies can be the limitations in the time coverage of the 2,299 UVES observations. Therefore, we selected a WACCM sample of the same size containing the averaged intensities of the model time steps in temporal agreement with each UVES observation. The resulting climatology is shown in Figure 3c. Overall, the main features are very similar to those for the full WACCM data set. The strong SAO with the oppositional nocturnal trends in June and January is clearly visible. Only the details of the variability pattern differ. This statement is further supported by a correlation coefficient  $r$  for both WACCM-related climatologies of 0.89. The results of the harmonic analysis in Table 1 are also very similar. Only the relative amplitude of the SAO for the selected time steps of about 12% appears to be somewhat smaller than the about 15% for all data. The  $a_2$ -to- $a_1$  ratio of  $3.09 \pm 0.62$  agrees within the uncertainties. Both WACCM-related climatologies show very small  $r$  of 0.14 (all data) and 0.12 (specific data set) for correlations with the UVES data. Hence, the time coverage of our sample of UVES spectra is not critical for the comparison of the K nightglow climatologies from observation and modeling. As illustrated by UVES-to-WACCM ratios between 0.26 and 1.00 in Figure 3d, the agreement is not good in any case.

The  $a_0$  coefficients for UVES and WACCM in Table 1 are significantly different. If our  $R_D$  estimate from section 4 is sufficiently precise, this would suggest an efficiency of the K nightglow generation of about 50%. We will further discuss this result in section 6.2.

### 5.2. Long-Term Variations

The solar cycle effect and long-term trend for K nightglow at Cerro Paranal can also be derived from our WACCM simulation with the same bilinear regression analysis as described in section 3.2. For the sample of WACCM time steps matching the UVES data, we found  $-7.4 \pm 1.3\%$  per 100 sfu and  $+4.1 \pm 1.3\%$  per decade. For the full WACCM nighttime data set for the period from 2000 to 2014, the results are  $-9.6 \pm 0.2\%$  per 100 sfu and  $-0.4 \pm 0.2\%$  per decade. The solar cycle effects for both WACCM data sets agree well with the one for the UVES-based  $K(D_1)$  intensities shown in Figure 5. The negative correlation is confirmed. In contrast, the sign and amount of the long-term trend are not clear as the UVES and two WACCM data sets differ here. In view of the large discrepancies for the climatologies discussed in section 5.1 and the relatively short period for long-term trend studies, it is questionable whether these differences are realistic.

Interestingly, an investigation of Dawkins et al. (2016) of the global long-term variations of the K column density  $N_K$  with free running WACCM for the period from 1955 to 2005 resulted in a solar cycle effect of  $-14.4 \pm 1.3\%$  per 100 sfu and a long-term trend of  $+3.1 \pm 0.5\%$  per decade for the latitude interval between the equator and  $30^\circ\text{S}$ . Moreover, the same study shows a much less negative solar forcing for the Na column density, which agrees with the differences between the Na and K nightglow intensities discussed in section 3.2. Hence, the presence of a negative solar cycle effect for K nightglow appears to be related to variations in the metal atom abundance, which is dominated by changes in the equilibrium between the metal atom and its reservoir species, that is, molecules and ions. According to Dawkins et al. (2016), the main driver for the negative solar cycle effect for  $N_K$  appears to be the higher photoionization rates for K atoms at high solar activity. These are accompanied by increased mesopause temperatures and higher photodissociation rates (causing higher O and  $\text{O}_3$  abundances). However, the impact of these changes on the ratio of KO to K depending on reactions (3) and (4) does not seem to produce a sufficiently positive solar cycle response to compensate for the increased ion abundances. In the case of Na, this is different since there is an additional pathway besides photodissociation for the production of the neutral atom by the reaction of  $\text{NaHCO}_3$  with atomic hydrogen (Dawkins et al., 2016; Plane et al., 2014).

## 6. Analysis of K Nightglow With Satellite Data

As discussed in section 5.1, the WACCM- and UVES-related K nightglow climatologies differ significantly. In order to better understand these discrepancies, we can analyze atomic and molecular abundances as well as temperatures needed to calculate the WACCM-related K nightglow production. For this purpose, we use appropriate profiles from satellite missions for the area around Cerro Paranal. Such data are also useful for an independent simulation of the  $K(D)$  intensity, which can be realized if the K chemistry from the WACCM-K model (Plane et al., 2014) is applied. As only the quantum yield of the K nightglow process remains unknown, a comparison with the  $R_D$ -corrected  $K(D_1)$  intensities from the UVES data indicates the amount of this quantity. For these two applications that are discussed in the following, we used data from OSIRIS and SABER (see section 1).

For the crucial K density profiles, we took the OSIRIS-based measurements from Dawkins et al. (2014, 2015) for the years 2004 to 2013. The K number densities ( $n_K$ ) are based on  $K(D_1)$  fluorescence intensities. Thus, the  $n_K$  retrieval involves measuring the intensity of solar-pumped resonance fluorescence from K atoms in the upper mesosphere. During daytime this signal completely dominates the D-line emission produced from the chemiluminescent reaction between KO and atomic oxygen. The  $n_K$  are available for the fixed LTs 06:00 and 18:00 when the Sun was above the horizon. As nighttime data are not available, we have to rely on a sufficiently small diurnal variation to keep the systematic bias low. Support for this is provided by comparisons of OSIRIS daytime K column densities with nighttime K lidar measurements at Arecibo ( $18^\circ\text{N}$ ) and K hlungsborn ( $54^\circ\text{N}$ ), which did not show significant systematic offsets (Dawkins et al., 2014). Lidar measurements during day and night at K hlungsborn (Feng et al., 2015; Lautenbach et al., 2017) indicate that the daylight and nighttime K densities should be similar on average with differences of less than 20% close to the layer peak. The minimum and maximum K densities tend to be found around dusk and dawn, respectively. In order to characterize Cerro Paranal, we considered the full latitude band between  $20^\circ\text{S}$  and  $30^\circ\text{S}$ . Additional constraints in longitude would have increased statistical uncertainties.

For the number densities of ozone ( $n_{\text{O}_3}$ ) and atomic oxygen ( $n_{\text{O}}$ ) as well as the kinetic temperature ( $T_{\text{kin}}$ ), which are involved in reactions (3) and (4), we used limb-sounding nighttime profiles from SABER (Russell et al., 1999) for the period from 2002 to 2014. We selected the most recent products related to Mlynczak et al. (2018), which are provided for 16 pressure levels between about 80 to 100 km. Ozone densities are retrieved from the prominent  $\text{O}_3$  band at  $9.6 \mu\text{m}$  (Smith et al., 2013) and  $T_{\text{kin}}$  are based on the  $\text{CO}_2$  emission at  $15 \mu\text{m}$  and modeling (Dawkins et al., 2018). Atomic oxygen is derived from OH nightglow emission (Mlynczak et al., 2013, 2018). Although the debate on the best retrieval approach is still ongoing (Fytterer et al., 2019; Panka et al., 2018; Zhu & Kaufmann, 2018), the systematic uncertainties in  $n_{\text{O}}$  appear to be sufficiently small for our study. The selection of the profiles for the different properties was restricted to an area around Cerro Paranal with maximum latitudinal and longitudinal deviations of  $5^\circ$  and  $10^\circ$ , respectively. Comparisons of northern and southern subsamples with respect to  $24.6^\circ\text{S}$  do not indicate significant qualitative changes in the variability patterns of the different properties; that is, the selected latitude range of  $10^\circ$  is sufficiently representative of Cerro Paranal. For the longitude range of  $20^\circ$ , this was already tested by Noll et al. (2016).

### 6.1. Discussion of Climatologies

The resulting 14,868 SABER profiles for  $n_{\text{O}_3}$ ,  $n_{\text{O}}$ , and  $T_{\text{kin}}$  were used to produce climatologies for different heights (derived in the same way as described in section 3.1). For an optimal comparison, the creation of the corresponding WACCM climatologies was based on the 99,736 nocturnal time steps for the years 2002 to 2014 as the SABER data archive starts in January 2002. In the following, we mainly focus on an altitude of 89 km, which corresponds to the mean centroid altitude of the WACCM-K nightglow layer at Cerro Paranal. This is about 2 km lower than the corresponding height for the K nightglow model based on OSIRIS and SABER data. As the full width at half maximum of the emission layer is at least 7 km and the vertical resolution of WACCM is 3.5 km, this discrepancy is not critical for the comparison displayed in Figure 7.

The SABER- and WACCM-based climatologies for ozone in Figures 7a and 7b show a strong SAO with maxima in April and October and weaker nocturnal trends. However, the SABER-related relative variations are much stronger (by a factor of about 3.5), and the nocturnal variability patterns disagree. The underestimation of the SAO in WACCM could explain the discrepancies in the seasonal K nightglow variations in Figure 3. The WACCM-related SAOs for  $\text{K}(\text{D}_1)$  and  $\text{O}_3$  are opposite in phase. With a stronger  $\text{O}_3$ -related SAO than in WACCM (as seen in the SABER data), the WACCM-related SAO in  $I_{\text{K}(\text{D}_1)}$  could be weakened significantly via a much higher KO production in reaction (3) around the equinoxes compared to the solstices; that is, the seasonal variations would be closer to the AO-dominated pattern found for the UVES data. For the correct phase of the AO, it is important that the SABER-related  $n_{\text{O}_3}$  in southern winter are higher than in summer. Figure 7c shows that  $n_{\text{O}_3}$  from SABER are always larger than those from WACCM. The factors are between 1 and 4. The underprediction of ozone in WACCM probably results from an underestimation of vertical transport due to systematic uncertainties in its parametrization (Smith et al., 2014). As the southern summer months around January show the lowest factors, they seem to be the most reliable ones of WACCM in terms of  $\text{O}_3$ . As discussed above, this period of the year also indicates the best agreement between the UVES and WACCM- $\text{K}(\text{D}_1)$  data with respect to the nocturnal intensity trends.

Atomic oxygen is expected to have a weaker impact on  $\text{K}(\text{D}_1)$  emission than  $\text{O}_3$  due to the orders of magnitude higher O densities in the mesopause region, which means that reaction (3) rather than reaction (4) is rate determining in the chemiluminescence cycle (e.g., Plane et al., 2015). Nevertheless, the SABER-related  $n_{\text{O}}$  at 89 km in Figure 7d show a good correlation ( $r = +0.67$ ) with the UVES-based  $I_{\text{K}(\text{D}_1)}$  in Figure 3a. The correlation coefficient maximizes for the slightly lower altitude of 87 km ( $r = +0.73$ ). Both variability patterns exhibit the highest values at the end of the night with the main maximum in June and a secondary one in October. As O is a useful tracer for the vertical dynamics due to the steep increase of the O volume mixing ratio with height below the mesopause (e.g., Smith et al., 2010), this result indicates that the  $I_{\text{K}(\text{D}_1)}$  maximum appears to coincide with strong downward transport of atomic oxygen. Interestingly, the data of Unterguggenberger et al. (2017) suggest that the correlation with O seems to be weaker for Na than for K nightglow. Compared to the SABER data, the WACCM-related  $n_{\text{O}}$  climatology in Figure 7e shows clear differences. It reveals a dominating SAO with maxima in April and November. However, strong nocturnal  $n_{\text{O}}$  increases are not present. As indicated by Figure 7f, this results in an underprediction of  $n_{\text{O}}$  by WACCM in the morning around June. For most parts of the climatology, the plotted ratios suggest an overprediction compared to the SABER O retrievals by Mlynczak et al. (2018). In any case, the high ratios in Figure 7f point to strong vertical motions in the mesopause region at Cerro Paranal, which are not sufficiently included in the WACCM simulation.

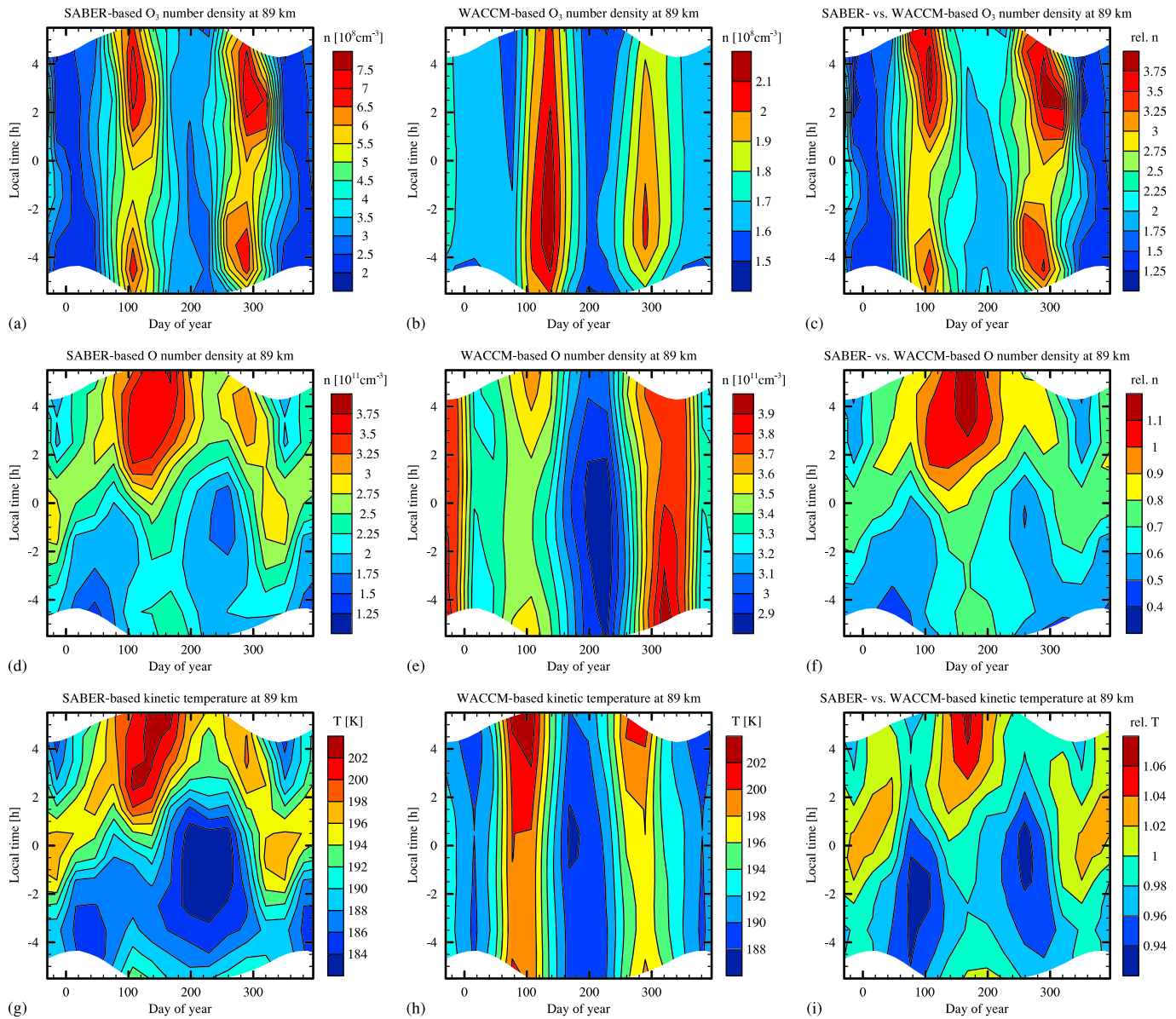


**Figure 7.** Contour plots of  $O_3$  number densities in  $10^8 \text{ cm}^{-3}$  (a–c), O number densities in  $10^{11} \text{ cm}^{-3}$  (d–f), and kinetic temperatures in K (g–i) at 89 km for Cerro Paranal and the period from 2002 to 2014 from the SABER products related to (a, d, and g) Mlynczak et al. (2018) and (b, e, and h) WACCM. The ratios of the SABER- and WACCM-based results are shown in the right column. The plots were created in the same way as described in Figure 3. SABER = Sounding of the Atmosphere using Broadband Emission Radiometry; WACCM = Whole Atmosphere Community Climate Model.

As  $O_3$  originates from the reaction of O with  $O_2$ , one might expect that the discrepancies in  $n_O$  would also be present in  $n_{O_3}$ . However, Figure 7c shows the strongest nocturnal increases around the equinoxes. The relative nocturnal trend in June is minimal with a maximum-to-minimum ratio of 1.1 compared to the values for the other months of up to 1.8. One factor contributing to the weak increase in June is the relatively strong temperature dependence of the ozone formation with a power of  $-2.4$  (Burkholder et al., 2015). The SABER  $T_{\text{kin}}$  climatology is plotted in Figure 7g. It shows a variability pattern that is very similar to the one for atomic oxygen ( $r = +0.94$ ), which indicates that tides and other waves should have an important impact on the present variations. As the WACCM  $T_{\text{kin}}$  data in Figure 7h only display a weak SAO and no noteworthy nocturnal trends, the ratio of the SABER and WACCM climatologies in Figure 7i reveals a maximum in the morning in June as in the case of  $n_O$ . The high positive  $T_{\text{kin}}$  offset in this period then reduces the ozone production by more than 20%, which partly explains the weak nocturnal trend in June in Figure 7c. The increased loss of ozone by reactions with atomic hydrogen at higher  $T_{\text{kin}}$  (Burkholder et al., 2015) also

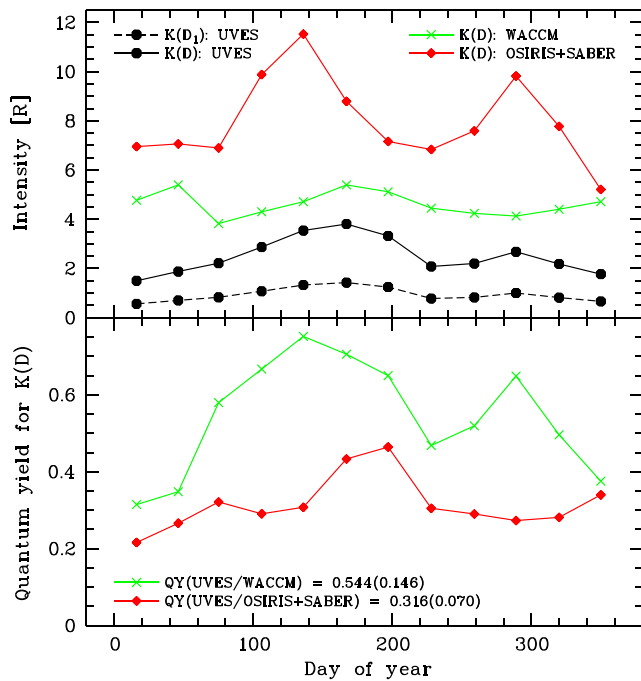


**Figure 8.** Derivation of quantum yield for K(D) emission with respect to the reaction of K with O<sub>3</sub> (QY<sub>K</sub>). The upper panel shows the monthly mean K(D) intensities for the UVES data from 2002 to 2014 (solid lines and filled circles), WACCM simulation from 2002 to 2014 (crosses), and model based on OSIRIS and SABER data (filled diamonds) as a function of the day of year. Moreover, the UVES-related monthly mean K(D<sub>1</sub>) intensities without a correction for K(D<sub>2</sub>) are displayed as dashed lines and filled circles. The lower panel shows the ratios of the monthly mean K(D) intensities for UVES and WACCM (crosses) as well as UVES and OSIRIS plus SABER (filled diamonds). These ratios indicate the quantum yield. The corresponding annual mean values and standard deviations derived from the monthly values are listed in the plot. UVES = Ultraviolet and Visual Echelle Spectrograph; WACCM = Whole Atmosphere Community Climate Model; OSIRIS = Optical Spectrograph and Infrared Imaging System; SABER = Sounding of the Atmosphere using Broadband Emission Radiometry.

contributes to this effect. Reactions (3) and (4) are only weakly temperature dependent (Plane et al., 2014). With the relatively small WACCM  $T_{kin}$  errors in Figure 7i, this possible temperature effect can be neglected.

Deviations of the WACCM simulations in the variability of the K concentrations may also contribute to the differences in the K nightglow climatologies in Figure 3. For the latitude of Cerro Paranal, a comparison of daytime WACCM and OSIRIS satellite data (Dawkins et al., 2015; Plane et al., 2015) indicates very similar seasonal variations. The K column densities agree very well in January. In June, those from OSIRIS appear to be about 50% higher, which indicates that the WACCM-K abundances also contribute to the large discrepancies for the WACCM  $I_{K(D_1)}$  seasonal variations, but less than the O<sub>3</sub> concentrations. For the nocturnal trends, there are no data (see beginning of section 6). However, the very dynamic situation in the morning in southern winter, which is not well predicted by WACCM, certainly also leads to a change of the properties of the K layer (see also section 6.2).

## 6.2. Quantum Yield

For the calculation of the K(D)-related quantum yield of the reaction of K with O<sub>3</sub> (QY<sub>K</sub>), we used monthly mean values of the 1,957 measured UVES-based K(D<sub>1</sub>) intensities for the period from 2002 to 2014 to match the SABER data set. The required K(D) intensities were then derived by applying the factor of 2.67 estimated in section 4. For each month, we also averaged the selected OSIRIS-based K density profiles and SABER-based profiles in ozone density and  $T_{kin}$  to calculate the production of KO by reaction (3), which gives us K(D) intensities for a reference QY<sub>K</sub> of 100% (cf. section 5). The seasonal variations of satellite- and UVES-based K nightglow intensities for Cerro Paranal are plotted in Figure 8. The satellite-based intensities show a dominating SAO with the main maximum in May and a weaker maximum in October. These positions roughly agree with those for the UVES data, where the corresponding maxima are in June and October (cf. Figure 4). The satellite-related October peak has a distinctly higher relative amplitude than in the case of UVES. Despite such differences, our reference model shows a much better agreement of the seasonal variations than the monthly mean K(D) intensities based on K + O<sub>3</sub> for the WACCM time steps related to the 1,957 UVES spectra, which are also shown in Figure 8. The WACCM data indicate maxima in February and June with similar but very small amplitudes.

The resulting quantum yields, that is, K(D) intensity ratios, are displayed in Figure 8 as well. The QY<sub>K</sub> percentages range from 22% in January to 46% in July. The corresponding annual mean is 32% with a standard deviation of 7% reflecting the monthly variations. The scatter can be reduced significantly if June and July, that is, the months with the highest apparent QY<sub>K</sub>, are not considered. In this case, mean and standard deviation are 29% and 3%, respectively. The discrepancies for June and July suggest that the strong downwelling situation in the morning hours at Cerro Paranal (section 6.1) may not be sufficiently mapped by the daytime OSIRIS K data for the latitudes between 15° and 35°S. In addition, these months are also those months with the longest nights with solar zenith angles above 100° for about 12 hr, which can be a problem for the OSIRIS measurements at 6:00 and 18:00 LT. Therefore, a QY<sub>K</sub> calculation without the affected months appears to be more realistic. Under this condition, the quantum yield for K(D<sub>1</sub>), which does not depend on our estimate of  $R_D$ , would be 10.8% with a scatter of 1.3%. Figure 8 also reveals the expected poor performance of the WACCM data for the QY<sub>K</sub> determination. The percentages range up to 72% (May). Mean and standard deviation are 54% and 15%, respectively. In section 6.1, it was concluded that the most reliable WACCM season seems to be southern summer and especially the month January, when the discrepancies in the ozone density with respect to SABER are minimal (a factor of 1.4 at 89 km in January). In this case, QY<sub>K</sub> would be 31% for January or 35% for summer, which agrees well with the result from the satellite-based approach.

We have defined  $QY_K$  with respect to reaction (3); that is,  $QY_K$  is the probability of K(D) emission when a K atom reacts with ozone. The reaction which is actually responsible for photon emission is reaction (4) between KO and atomic oxygen, for which the quantum yield  $QY_{KO}$  is given by the ratio of the resulting excited  $^2P_J$  states with subsequent photon emission to all K states. If all KO molecules produced by reaction (3) went on to react with atomic oxygen and there were no other sources of KO, then  $QY_K$  would be equal to  $QY_{KO}$ . However, as KO can also be produced by reactions (5) and (6) involving  $KO_2$  (Plane et al., 2014; Swider, 1987),  $QY_K$  is overestimated in comparison to  $QY_{KO}$ . Note that although KO is also removed by reactions with  $O_3$ ,  $H_2O$ , and  $H_2$ , which do not produce K(D) emission (Plane et al., 2014), these removal processes are very slow compared to reaction with O, and so have essentially no impact on the quantum yield. This is because the concentration of O is at least 100 times larger, and these reactions all have similar rate coefficients. The WACCM results show that  $QY_{KO}$  is on average 10.2% smaller than  $QY_K$  with a standard deviation of 2.6%, which implies a contribution of the  $KO_2$ -related reaction pathway that is only half as large as estimated by Swider (1987). For January,  $QY_{KO}$  is 27%. If we assume that the monthly ratios for both quantum yields are also valid for the satellite-based results, we obtain  $QY_{KO}$  percentages of  $28 \pm 7\%$  for the whole year and  $26 \pm 3\%$  for all months excluding June and July. The latter is half as large as the simple purely statistical estimate in section 4 based on the pathways for  $KO(^2\Sigma_{1/2} \text{ and } ^2\Pi_{3/2}) + O$  in Figure 6, which resulted in a  $QY_{KO}$  of 50%. A likely reason for this is that production of  $K(^2P_J)$  requires a strikingly large fraction (71%) of the energy released by reaction (4) to go into electronic excitation of K. A  $K(D_1)$  photon has an energy of 155 kJ/mol, whereas the reaction between KO and O is exothermic by only 217 kJ/mol (Figure 6).

Despite the nonnegligible uncertainties, a quantum yield of about 30% is significantly higher than those for other reactions of metals with ozone. Based on Cerro Paranal spectroscopic data and WACCM simulations, Unterguggenberger et al. (2017) found a quantum yield of  $11 \pm 2\%$  for Na(D) emission and  $13 \pm 3\%$  for the FeO pseudocontinuum. As these estimates are related to the whole year and not only southern summer, Figure 8 indicates that the discrepancies should even be larger. Note that the much higher quantum yield for K compared with Na is not explained by statistical consideration of the potential energy surfaces correlating with the excited metal atom products. In the case of Na, this would indicate a quantum yield of 33% (Plane et al., 2012), about 3 times higher than observed by Unterguggenberger et al. (2017).

## 7. Conclusions

Using high-resolution spectroscopy with the astronomical UVES echelle spectrograph at Cerro Paranal in Chile (24.6°S, 70.4°W) for the period from 2000 to 2014, we studied a sample of 2,299 nighttime intensity measurements of the  $K(D_1)$  line. The mean intensity of about 0.95 R agrees well with the previous measurement by Slangier and Osterbrock (2000) for Mauna Kea in Hawaii. In order to estimate the intensity of the almost fully absorbed  $K(D_2)$  line relative to  $K(D_1)$ , we considered the electronic potential energy surfaces related to the reactions  $KO(X^2\Sigma) + O$  and  $KO(A^2\Pi) + O$  and found a factor of 1.67. Hence, the K(D) mean intensity including both lines should be about 2.5 R. For the first time, the variability of chemiluminescent K emission has been investigated. The  $K(D_1)$  climatology reveals a dominating AO with an amplitude  $a_1$  of about 30% and the maximum in June. A minor secondary maximum is present in October. The emission tends to increase during the night, especially in June, when an intensity of almost 2 R is achieved before dawn. This remarkable climatological maximum is also visible in the O density from the SABER limb-sounding radiometer for Cerro Paranal around 90 km and below, suggesting strong downward motions. A regression analysis of the long-term variations revealed a significant negative correlation with the solar activity of  $-11 \pm 3\%$  per 100 sfu, whereas the covered period is not long enough to derive a clear linear long-term trend.

We then used the WACCM-K model to simulate K nightglow emission at Cerro Paranal with a time resolution of 30 min for the years from 2000 to 2014. The modeled variations turned out to be different from the measured ones. In contrast to the UVES data, a SAO with maxima in January and July is dominant. The ratio of the amplitudes  $a_2$  and  $a_1$  is about 3.4 compared to about 0.6 for the measured intensities. Moreover, the intensity does not increase during the night in the middle of the year. Nevertheless, the nocturnal trends for the UVES and WACCM samples are similar around January in southern summer. The higher quality of the WACCM simulation for this period is also indicated by a comparison of the  $O_3$  densities, O densities, and temperatures from WACCM and SABER at 89 km for Cerro Paranal. The SABER-related  $O_3$  densities are always higher but only a factor of about 1.4 for January compared to values above 3 around the equinoxes in

the second half of the night. The worst agreement in terms of O density and temperature was found in the morning around June, where the SABER-to-WACCM ratios are distinctly higher than for other times and seasons. The long-term variations of the WACCM-based K(D) intensities were also investigated. The solar cycle effect agrees well with the one from the UVES data, although the sign of the long-term trend is uncertain for the 15 years. The main reason for the negative solar forcing is probably related to a higher K ion fraction during periods of high solar activity.

Finally, we derived for the first time the quantum yield of the reaction of K and O<sub>3</sub> (i.e., the production of KO) with respect to the production of K nightglow. For this purpose, we combined SABER profiles and OSIRIS K density data to calculate monthly reference K(D) intensities for a quantum yield of 100%. Comparison with the corresponding UVES-based K(D<sub>1</sub>) data corrected for the K(D<sub>2</sub>) line indicates an annual average of  $32 \pm 7\%$ . Without the least reliable months June and July (due to limitations in the OSIRIS data), the quantum yield is  $29 \pm 3\%$ . For the most trustworthy month January of the WACCM simulation, we found 31%. As KO can also be produced by the reaction of KO<sub>2</sub> with atomic oxygen, we used the WACCM data to estimate this contribution. The resulting quantum yields are about 10% lower on average. For the satellite-based mean quantum yield excluding June and July, this corresponds to  $26 \pm 3\%$ . This percentage is about 2 times lower than a simple statistical estimate of 50% based on reactive surfaces correlating KO + O with K(<sup>2</sup>P) under mesospheric conditions.

K nightglow behaves very differently from Na nightglow, although both atoms are alkali metals with the same meteoric ablation origin. Compared with Na, conspicuous deviations are found for the seasonal variations (stronger AO), solar cycle effect (more negative correlation), and quantum yield (at least 3 times larger). The reasons that these alkali metals behave so differently are not obvious.

#### Acknowledgments

S. Noll is financed by the project NO 1328/1-1 of the German Research Foundation (DFG). J. M. C. Plane and W. Feng were funded by the European Research Council (project 291332-CODITA). W. Kausch is funded by the Hochschulraumstrukturmittel provided by the Austrian Federal Ministry of Education, Science and Research (BMBWF). We thank the two anonymous reviewers for their detailed and very helpful comments. This project made use of the ESO Science Archive Facility at the ESO website (<http://archive.eso.org>). UVES Phase 3 spectra from different observing programs of the period from April 2000 to March 2015 were analyzed. The SABER nighttime data products related to Mlynczak et al. (2018) were taken from the SABER website (<http://saber.gats-inc.com>). Basic OSIRIS data products are accessible via a website (<https://arg.usask.ca/projects/osiris>). The WACCM-K data set generated for this work has been archived at the Leeds University PetaByte Environmental Tape Archive and Library (PETAL; <https://www.environment.leeds.ac.uk/wiki/view/IT/PetalArchive>) and is available from J. M. C. Plane or W. Feng. Moreover, all data relevant for the figures of this paper are provided as supporting information.

#### References

- Burkholder, J. B., Sander, S. P., Abbatt, J., Barker, J. R., Huie, R. E., Kolb, C. E., et al. (2015). *Chemical kinetics and photochemical data for use in atmospheric studies, evaluation No. 18, JPL Publ 15-10*. Pasadena: Jet Propulsion Laboratory.
- Chapman, S. (1939). Notes on atmospheric sodium. *The Astrophysical Journal*, *90*, 309. <https://doi.org/10.1086/144109>
- Clough, S. A., Shephard, M. W., Mlawer, E. J., Delamere, J. S., Iacono, M. J., Cady-Pereira, K., et al. (2005). Atmospheric radiative transfer modeling: A summary of the AER codes. *Journal of Quantitative Spectroscopy & Radiative Transfer*, *91*, 233–244. <https://doi.org/10.1016/j.jqsrt.2004.05.058>
- Cosby, P. C., Sharpee, B. D., Slinger, T. G., Huestis, D. L., & Hanuschik, R. W. (2006). High-resolution terrestrial nightglow emission line atlas from UVES/VLT: Positions, intensities, and identifications for 2808 lines at 314–1043 nm. *Journal of Geophysical Research*, *111*, A12307. <https://doi.org/10.1029/2006JA012023>
- Dawkins, E. C. M., Feofilov, A., Rezac, L., Kutepov, A. A., Janches, D., Höffner, J., et al. (2018). Validation of SABER v2.0 operational temperature data with ground-based lidars in the mesosphere-lower thermosphere region (75–105 km). *Journal of Geophysical Research: Atmospheres*, *123*, 9916–9934. <https://doi.org/10.1029/2018JD028742>
- Dawkins, E. C. M., Plane, J. M. C., Chipperfield, M. P., & Feng, W. (2015). The near-global mesospheric potassium layer: Observations and modeling. *Journal of Geophysical Research: Atmospheres*, *120*, 7975–7987. <https://doi.org/10.1002/2015JD023212>
- Dawkins, E. C. M., Plane, J. M. C., Chipperfield, M. P., Feng, W., Gumbel, J., Hedin, J., et al. (2014). First global observations of the mesospheric potassium layer. *Geophysical Research Letters*, *41*, 5653–5661. <https://doi.org/10.1002/2014GL060801>
- Dawkins, E. C. M., Plane, J. M. C., Chipperfield, M. P., Feng, W., Marsh, D. R., Höffner, J., & Janches, D. (2016). Solar cycle response and long-term trends in the mesospheric metal layers. *Journal of Geophysical Research: Space Physics*, *121*, 7153–7165. <https://doi.org/10.1002/2016JA022522>
- Dekker, H., D'Odorico, S., Kaufer, A., Delabre, B., & Kotzlowski, H. A. F. (2000). Design, construction, and performance of UVES, the echelle spectrograph for the UT2 Kueyen Telescope at the ESO Paranal Observatory. *Proceedings of SPIE*, *4008*, 534–545. <https://doi.org/10.1117/12.395512>
- Eska, V., Höffner, J., & von Zahn, U. (1998). Upper atmosphere potassium layer and its seasonal variations at 54°N. *Journal of Geophysical Research*, *103*, 29,207–29,214. <https://doi.org/10.1029/98JA02481>
- Fan, Z. Y., Plane, J. M. C., Gumbel, J., Stegman, J., & Llewellyn, E. J. (2007). Satellite measurements of the global mesospheric sodium layer. *Atmospheric Chemistry and Physics*, *7*, 4107–4115.
- Felix, F., Keenlside, W., & Kent, G. (1973). Laser radar observations of atmospheric potassium. *Nature*, *246*, 345–346. <https://doi.org/10.1038/246345a0>
- Feng, W., Höffner, J., Marsh, D. R., Chipperfield, M. P., Dawkins, E. C. M., Viehl, T. P., & Plane, J. M. C. (2015). Diurnal variation of the potassium layer in the upper atmosphere. *Geophysical Research Letters*, *42*, 3619–3626. <https://doi.org/10.1002/2015GL063718>
- Friedman, J. S., Collins, S. C., Delgado, R., & Castleberg, P. A. (2002). Mesospheric potassium layer over the Arecibo Observatory, 18.366.75°W. *Geophysical Research Letters*, *29*(5), 1071. <https://doi.org/10.1029/2001GL013542>
- Frisch, M. J., Trucks, G. W., Schlegel, H. B., Scuseria, G. E., Robb, M. A., Cheeseman, J. R., et al. (2016). Gaussian 16 Revision B.01, Gaussian Inc. Wallingford, CT USA.
- Fytterer, T., von Savigny, C., Mlynczak, M., & Sinnhuber, M. (2019). Model results of OH airglow considering four different wavelength regions to derive night-time atomic oxygen and atomic hydrogen in the mesopause region. *Atmospheric Chemistry and Physics*, *19*, 1835–1851. <https://doi.org/10.5194/acp-19-1835-2019>
- Garcia, R. R., Marsh, D. R., Kinnison, D. E., Boville, B. A., & Sassi, F. (2007). Simulation of secular trends in the middle atmosphere, 1950–2003. *Journal of Geophysical Research*, *112*, D09301. <https://doi.org/10.1029/2006JD007485>



- Gardner, C. S., Plane, J. M. C., Pan, W., Vondrak, T., Murray, B. J., & Chu, X. (2005). Seasonal variations of the Na and Fe layers at the South Pole and their implications for the chemistry and general circulation of the polar mesosphere. *Journal of Geophysical Research*, *110*, D10302. <https://doi.org/10.1029/2004JD005670>
- Hanuschik, R. W. (2003). A flux-calibrated, high-resolution atlas of optical sky emission from UVES. *Astronomy & Astrophysics*, *407*, 1157–1164. <https://doi.org/10.1051/0004-6361:20030885>
- Höffner, J., & Lübken, F. J. (2007). Potassium lidar temperatures and densities in the mesopause region at Spitsbergen (78°N). *Journal of Geophysical Research*, *112*, D20114. <https://doi.org/10.1029/2007JD008612>
- Huber, K. P., & Herzberg, G. (1979). *Molecular spectra and molecular structure. IV Constants of diatomic molecules*. New York: Van Nostrand Reinhold. <https://doi.org/10.1007/978-1-4757-0961-2>
- Hurrell, J. W., Holland, M. M., Gent, P. R., Ghan, S., Kay, J. E., Kushner, P. J., et al. (2013). The Community Earth System Model: A framework for collaborative research. *Bulletin of the American Meteorological Society*, *94*, 1339–1360. <https://doi.org/10.1175/BAMS-D-12-00121.1>
- Kinnison, D. E., Brasseur, G. P., Walters, S., Garcia, R. R., Marsh, D. R., Sassi, F., et al. (2007). Sensitivity of chemical tracers to meteorological parameters in the MOZART-3 chemical transport model. *Journal of Geophysical Research*, *112*, D20302. <https://doi.org/10.1029/2006JD007879>
- Lamarque, J.-F., Emmons, L. K., Hess, P. G., Kinnison, D. E., Tilmes, S., Vitt, F., et al. (2012). CAM-chem: Description and evaluation of interactive atmospheric chemistry in the Community Earth System Model. *Geoscientific Model Development*, *5*, 369–411. <https://doi.org/10.5194/gmd-5-369-2012>
- Langowski, M. P., von Savigny, C., Burrows, J. P., Fussen, D., Dawkins, E. C. M., Feng, W., et al. (2017). Comparison of global datasets of sodium densities in the mesosphere and lower thermosphere from GOMOS, SCIAMACHY and OSIRIS measurements and WACCM model simulations from 2008 to 2012. *Atmospheric Measurement Techniques*, *10*, 2989–3006. <https://doi.org/10.5194/amt-10-2989-2017>
- Lautenbach, J., Höffner, J., Lübken, F. J., Kopp, M., & Gerding, M. (2017). Ten-year climatology of potassium number density at 54°N, 12°E. *Journal of Atmospheric and Solar-Terrestrial Physics*, *162*, 172–177. <https://doi.org/10.1016/j.jastp.2017.06.010>
- Lee, E. P. F., Soldán, P., & Wright, T. G. (2002). What is the ground electronic state of KO. *The Journal of Chemical Physics*, *117*, 8241–8247. <https://doi.org/10.1063/1.1511179>
- Marsh, D. R., Mills, M. J., Kinnison, D. E., Lamarque, J.-F., Calvo, N., & Polvani, L. M. (2013). Climate change from 1850 to 2005 simulated in CESM1 (WACCM). *Journal Climate*, *26*, 7372–7391. <https://doi.org/10.1175/JCLI-D-12-00558.1>
- Mlynczak, M. G., Hunt, L. A., Mast, J. C., Thomas Marshall, B., Russell, J. M., Smith, A. K., et al. (2013). Atomic oxygen in the mesosphere and lower thermosphere derived from SABER: Algorithm theoretical basis and measurement uncertainty. *Journal of Geophysical Research: Atmospheres*, *118*, 5724–5735. <https://doi.org/10.1002/jgrd.50401>
- Mlynczak, M. G., Hunt, L. A., Russell, J. M., & Marshall, B. T. (2018). Updated SABER night atomic oxygen and implications for SABER ozone and atomic hydrogen. *Geophysical Research Letters*, *45*, 5735–5741. <https://doi.org/10.1029/2018GL077377>
- Neale, R. B., Chen, C. C., Gettelman, A., Lauritzen, P. H., Park, S., Williamson, D. L., et al. (2012). Description of the NCAR Community Atmosphere Model (CAM 5.0). NCAR Tech. Note NCAR/TN-486+STR, National Center for Atmospheric Research Boulder, CO USA.
- Noll, S., Kausch, W., Barden, M., Jones, A. M., Szyszka, C., Kimeswenger, S., & Vinther, J. (2012). An atmospheric radiation model for Cerro Paranal. I. The optical spectral range. *Astronomy & Astrophysics*, *543*, A92. <https://doi.org/10.1051/0004-6361/201219040>
- Noll, S., Kausch, W., Kimeswenger, S., Unterguggenberger, S., & Jones, A. M. (2015). OH populations and temperatures from simultaneous spectroscopic observations of 25 bands. *Atmospheric Chemistry and Physics*, *15*, 3647–3669. <https://doi.org/10.5194/acp-15-3647-2015>
- Noll, S., Kausch, W., Kimeswenger, S., Unterguggenberger, S., & Jones, A. M. (2016). Comparison of VLT/X-shooter OH and O<sub>2</sub> rotational temperatures with consideration of TIMED/SABER emission and temperature profiles. *Atmospheric Chemistry and Physics*, *16*, 5021–5042. <https://doi.org/10.5194/acp-16-5021-2016>
- Noll, S., Kimeswenger, S., Proxauf, B., Unterguggenberger, S., Kausch, W., & Jones, A. M. (2017). 15 years of VLT/UVES OH intensities and temperatures in comparison with TIMED/SABER data. *Journal of Atmospheric and Solar-Terrestrial Physics*, *163*, 54–69. <https://doi.org/10.1016/j.jastp.2017.05.012>
- Noll, S., Proxauf, B., Kausch, W., & Kimeswenger, S. (2018). Mechanisms for varying non-LTE contributions to OH rotational temperatures from measurements and modelling I. Climatology. *Journal of Atmospheric and Solar-Terrestrial Physics*, *175*, 87–99. <https://doi.org/10.1016/j.jastp.2018.05.004>
- Osterbrock, D. E., Fulbright, J. P., Cosby, P. C., & Barlow, T. A. (1998). Faint OH ( $v' = 10$ ), <sup>17</sup>OH, and <sup>18</sup>OH emission lines in the spectrum of the night airglow. *Publications of the Astronomical Society of the Pacific*, *110*, 1499–1510. <https://doi.org/10.1086/316272>
- Osterbrock, D. E., Fulbright, J. P., Martel, A. R., Keane, M. J., Trager, S. C., & Basri, G. (1996). Night-sky high-resolution spectral atlas of OH and O<sub>2</sub> emission lines for echelle spectrograph wavelength calibration. *Publications of the Astronomical Society of the Pacific*, *108*, 277. <https://doi.org/10.1086/133722>
- Osterbrock, D. E., Waters, R. T., Barlow, T. A., Slanger, T. G., & Cosby, P. C. (2000). Faint emission lines in the blue and red spectral regions of the night airglow. *Publications of the Astronomical Society of the Pacific*, *112*, 733–741. <https://doi.org/10.1086/316568>
- Panka, P. A., Kutepov, A. A., Rezac, L., Kalogerakis, K. S., Feofilov, A. G., Marsh, D., et al. (2018). Atomic oxygen retrieved from the SABER 2.0- and 1.6-radiances using new first-principles nighttime OH( $v$ ) model. *Geophysical Research Letters*, *45*, 5798–5803. <https://doi.org/10.1029/2018GL077677>
- Plane, J. M. C. (2012). Cosmic dust in the Earth's atmosphere. *Chemical Society Reviews*, *41*, 6507–6518. <https://doi.org/10.1039/c2cs35132c>
- Plane, J. M. C., Feng, W., & Dawkins, E. C. M. (2015). The mesosphere and metals: Chemistry and changes. *Chemical Reviews*, *115*(10), 4497–4541. <https://doi.org/10.1021/cr500501m>
- Plane, J. M. C., Feng, W., Dawkins, E., Chipperfield, M. P., Höffner, J., Janches, D., & Marsh, D. R. (2014). Resolving the strange behavior of extraterrestrial potassium in the upper atmosphere. *Geophysical Research Letters*, *41*, 4753–4760. <https://doi.org/10.1002/2014GL060334>
- Plane, J., Oetjen, H., de Miranda, M., Saiz-Lopez, A., Gausa, M., & Williams, B. (2012). On the sodium D line emission in the terrestrial nightglow. *Journal of Atmospheric and Solar-Terrestrial Physics*, *74*, 181–188. <https://doi.org/10.1016/j.jastp.2011.10.019>
- Russell, J. M. III, Mlynczak, M. G., Gordley, L. L., Tansock, J., & Esplin, R. (1999). Overview of the SABER experiment and preliminary calibration results. *Proceedings of SPIE*, *3756*, 277–288. <https://doi.org/10.1117/12.366382>
- Sansonetti, J. E. (2008). Wavelengths, transition probabilities, and energy levels for the spectra of potassium (K I through K XIX). *Journal of Physical and Chemical Reference Data*, *37*, 7–96. <https://doi.org/10.1063/1.2789451>
- Slanger, T. G., Cosby, P. C., Huestis, D. L., Saiz-Lopez, A., Murray, B. J., O'Sullivan, D. A., et al. (2005). Variability of the mesospheric nightglow sodium D<sub>2</sub>/D<sub>1</sub> ratio. *Journal of Geophysical Research*, *110*, D23302. <https://doi.org/10.1029/2005JD006078>
- Slanger, T. G., & Osterbrock, D. E. (2000). Investigations of potassium, lithium, and sodium emission in the nightglow and OH cross calibration. *Journal of Geophysical Research*, *105*, 1425–1430. <https://doi.org/10.1029/1999JD901027>

- Slipher, V. M. (1929). Emissions in the spectrum of the light of the night sky. *Publications of the Astronomical Society of the Pacific*, *41*, 262–263.
- Smith, A. K., Harvey, V. L., Mlynczak, M. G., Funke, B., Garcia-Comas, M., Hervig, M., et al. (2013). Satellite observations of ozone in the upper mesosphere. *Journal of Geophysical Research: Atmospheres*, *118*, 5803–5821. <https://doi.org/10.1002/jgrd.50445>
- Smith, A. K., López-Puertas, M., Funke, B., Garcia-Comas, M., Mlynczak, M. G., & Holt, L. A. (2014). Nighttime ozone variability in the high latitude winter mesosphere. *Journal of Geophysical Research: Atmospheres*, *119*, 13,547–13,564. <https://doi.org/10.1002/2014JD021987>
- Smith, A. K., Marsh, D. R., Mlynczak, M. G., & Mast, J. C. (2010). Temporal variations of atomic oxygen in the upper mesosphere from SABER. *Journal of Geophysical Research*, *115*, D18309. <https://doi.org/10.1029/2009JD013434>
- States, R. J., & Gardner, C. S. (1999). Structure of the mesospheric Na layer at 40°N latitude: Seasonal and diurnal variations. *Journal of Geophysical Research*, *104*, 11,783–11,798. <https://doi.org/10.1029/1999JD900002>
- Sullivan, H. M., & Hunten, D. M. (1962). Relative abundance of lithium, sodium and potassium in the upper atmosphere. *Nature*, *195*, 589–590. <https://doi.org/10.1038/195589a0>
- Swider, W. (1987). Chemistry of mesospheric potassium and its different seasonal behavior as compared to sodium. *Journal of Geophysical Research*, *92*, 5621–5626. <https://doi.org/10.1029/JD092iD05p05621>
- Tapping, K. F. (2013). The 10.7 cm solar radio flux ( $F_{10.7}$ ). *Space Weather*, *11*, 394–406. <https://doi.org/10.1002/swe.20064>
- Unterguggenberger, S., Noll, S., Feng, W., Plane, J. M. C., Kausch, W., Kimeswenger, S., et al. (2017). Measuring FeO variation using astronomical spectroscopic observations. *Atmospheric Chemistry and Physics*, *17*, 4177–4187. <https://doi.org/10.5194/acp-17-4177-2017>
- van Rhijn, P. J. (1921). On the brightness of the sky at night and the total amount of starlight. *Publ. Kapteyn Astron. Lab. Groningen*, *31*, 1–83.
- Vasiliiu, M., Li, S., Peterson, K. A., Feller, D., Gole, J. L., & Dixon, D. A. (2010). Structures and heats of formation of simple alkali metal compounds: Hydrides, chlorides, fluorides, hydroxides, and oxides for Li, Na, and K. *The Journal of Physical Chemistry*, *114*, 4272–4281. <https://doi.org/10.1021/jp911735c>
- von Savigny, C., Langowski, M. P., Zilker, B., Burrows, J. P., Fussen, D., & Sofieva, V. F. (2016). First mesopause Na retrievals from satellite Na D-line nightglow observations. *Geophysical Research Letters*, *43*, 12,651–12,658. <https://doi.org/10.1002/2016GL071313>
- von Zahn, U., & Höffner, J. (1996). Mesopause temperature profiling by potassium lidar. *Geophysical Research Letters*, *23*, 141–144. <https://doi.org/10.1029/95GL03688>
- Wang, Z., Yang, G., Wang, J., Yue, C., Yang, Y., Jiao, J., et al. (2017). Seasonal variations of meteoric potassium layer over Beijing (40.41°N, 116.01°E). *Journal of Geophysical Research: Space Physics*, *122*, 2106–2118. <https://doi.org/10.1002/2016JA023216>
- Yi, F., Yu, C., Zhang, S., Yue, X., He, Y., Huang, C., et al. (2009). Seasonal variations of the nocturnal mesospheric Na and Fe layers at 30°N. *Journal of Geophysical Research*, *114*, D01301. <https://doi.org/10.1029/2008JD010344>
- Yue, X., Friedman, J. S., Wu, X., & Zhou, Q. H. (2017). Structure and seasonal variations of the nocturnal mesospheric K layer at Arecibo. *Journal of Geophysical Research: Atmospheres*, *122*, 7260–7275. <https://doi.org/10.1002/2017JD026541>
- Zhu, Y., & Kaufmann, M. (2018). Atomic oxygen abundance retrieved from SCIAMACHY hydroxyl nightglow measurements. *Geophysical Research Letters*, *45*, 9314–9322. <https://doi.org/10.1029/2018GL079259>